Received: 24 June 2019 | Revised: 15 September 2019 | Accepted: 7 October 2019

DOI: 10.1002/mrm.28053

NOTE

Magnetic Resonance in Medicine

ActiveAx$_{ADD}$: Toward non-parametric and orientationally invariant axon diameter distribution mapping using PGSE

David Romascano[1,2] | **Muhamed Barakovic**[1] | **Jonathan Rafael-Patino**[1] | **Tim Bjørn Dyrby**[2,3] | **Jean-Philippe Thiran**[1,4] | **Alessandro Daducci**[1,4,5]

[1]Signal Processing Laboratory (LTS5), École Polytechnique Fédérale de Lausanne (EPFL), Lausanne, Vaud, Switzerland

[2]Danish Research Centre for Magnetic Resonance, Center for Functional and Diagnostic Imaging and Research, Copenhagen University Hospital Hvidovre, Hvidovre, Denmark

[3]Department of Applied Mathematics and Computer Science, Technical University of Denmark, Kongens Lyngby, Denmark

[4]Department of Radiology, University Hospital Center (CHUV) and University of Lausanne (UNIL), Lausanne, Vaud, Switzerland

[5]Computer Science Department, University of Verona, Verona, Italy

Correspondence
David Romascano, LTS5, STI, EPFL, Lausanne, Vaud, 1015, Switzerland.
Email: david.romascano@epfl.ch

Funding information
Swiss National Science Foundation (SNSF), Grant/Award Number: 31003A_157063.

Purpose: Non-invasive axon diameter distribution (ADD) mapping using diffusion MRI is an ill-posed problem. Current ADD mapping methods require knowledge of axon orientation before performing the acquisition. Instead, ActiveAx uses a 3D sampling scheme to estimate the orientation from the signal, providing orientationally invariant estimates. The mean diameter is estimated instead of the distribution for the solution to be tractable. Here, we propose an extension (ActiveAx$_{ADD}$) that provides non-parametric and orientationally invariant estimates of the whole distribution.

Theory: The accelerated microstructure imaging with convex optimization (AMICO) framework accelerates mean diameter estimation using a linear formulation combined with Tikhonov regularization to stabilize the solution. Here, we implement a new formulation (ActiveAx$_{ADD}$) that uses Laplacian regularization to provide robust estimates of the whole ADD.

Methods: The performance of ActiveAx$_{ADD}$ was evaluated using Monte Carlo simulations on synthetic white matter samples mimicking axon distributions reported in histological studies.

Results: ActiveAx$_{ADD}$ provided robust ADD reconstructions when considering the isolated intra-axonal signal. However, our formulation inherited some common microstructure imaging limitations. When accounting for the extra axonal compartment, estimated ADDs showed spurious peaks and increased variability because of the difficulty of disentangling intra and extra axonal contributions.

Conclusion: Laplacian regularization solves the ill-posedness regarding the intra axonal compartment. ActiveAx$_{ADD}$ can potentially provide non-parametric and orientationally invariant ADDs from isolated intra-axonal signals. However, further work is required before ActiveAx$_{ADD}$ can be applied to real data containing extra-axonal contributions, as disentangling the 2 compartment appears to be an overlooked challenge that affects microstructure imaging methods in general.

KEYWORDS
axon diameter, diffusion MRI, distribution, extra-axonal, intra-axonal, PGSE

1 | INTRODUCTION

White matter (WM) is composed of axon bundles (fascicles). Fascicles contain axons of different diameters,[1,2] forming an axon diameter distribution (ADD) that influences the speed of action potentials.[3,4] Different fascicles have different ADDs, which change during normal development,[5] but also during pathological events involving axonal degeneration and injury like multiple sclerosis,[6-9] amyotrophic lateral sclerosis,[10,11] Alzheimer's disease,[12] traumatic brain injury,[13] or stroke.[14]

Diffusion magnetic resonance imaging (dMRI) can be used to estimate tissue microstructural properties non-invasively. To estimate the ADD, WM fascicles are modeled as impermeable cylinders. ADD estimation is a challenging task, partly because similarly sized cylinders have similar dMRI signals, especially when using pulsed gradient spin echo (PGSE) sequences.[15] Small variations in the measurements (e.g., because of noise) can therefore drastically change the estimated ADD. To address these issues, several methods have been proposed (Table 1).

AxCaliber[16] provides parametric ADD estimates and is considered to be orientation-dependent because it requires the measurements to be acquired perpendicularly to the axons. To provide orientationally invariant features, the ActiveAx framework[17] acquires data using shells (i.e., 3D sampling schemes with many orientations covering the unit sphere), which allows the axon orientation to be estimated from the acquired dMRI signal.[17,18] For the acquisition time to remain feasible, ActiveAx uses the minimal model for WM diffusion ($\text{ActiveAx}_{\text{MMWMD}}$) that estimates the mean diameter index instead of the whole ADD, reducing the number of required shells. An ActiveAx protocol with 3 shells has been optimized for mean diameter mapping on ex vivo samples, with $G_{max} = 300$ mT/m.[19]

Daducci et al[20] proposed the accelerated microstructure imaging using convex optimization (AMICO) framework to linearize and accelerate the fitting of the $\text{ActiveAx}_{\text{MMWMD}}$ model. The linearized model ($\text{ActiveAx}_{\text{AMICO}}$) uses a formulation that is similar to the one used by Hollingsworth and Johns[21] and Benjamini et al[22] to estimate non-parametric distributions. Hollingsworth and Johns[21] first combined it with Laplacian regularization to estimate distribution of diameters of oil droplets in water. Benjamini et al[22] showed it could be used to provide non-parametric ADD estimates, using double diffusion encoding (DDE) instead of PGSE to increase stability. The acquisition had to be performed perpendicularly to the axons and is considered to be orientation-dependent.[22] The aim of this work is to show that the orientationally invariant features of $\text{ActiveAx}_{\text{AMICO}}$ can be combined with Laplacian regularization into a new formulation ($\text{ActiveAx}_{\text{ADD}}$) to reconstruct orientationally invariant and non-parametric estimates of the whole ADD using a PGSE protocol. The quality of the reconstructions was assessed using Monte Carlo simulations. Experiments demonstrated that Laplacian regularization allows providing robust ADDs from the isolated intra axonal (IA) signal, without the need of using DDE. However, the performance degraded when considering the extra axonal (EA) compartment. We show that the EA compartment might affect microstructure models in general, and further work is required before applying $\text{ActiveAx}_{\text{ADD}}$ to real data.

2 | THEORY

In the field of axon diameter mapping, axons are assumed to be impermeable cylinders.[16,17,22] The WM dMRI signal $\mathbf{S}$ is expressed as a weighted contribution of IA and EA signals[23]

$$\mathbf{S} = \mathbf{S}_0 * \left[f_{\text{IA}} \mathbf{S}_{\text{IA}} + (1 - f_{\text{IA}}) \mathbf{S}_{\text{EA}} \right] + \varepsilon, \quad (1)$$

where $\mathbf{S}_0$ is the MRI signal without diffusion weighting, f_{IA} is the IA volume fraction (IAVF), $\mathbf{S}_{\text{IA}}$ is the restricted IA signal,[24] $\mathbf{S}_{\text{EA}}$ is the hindered EA signal, and ε is the acquisition noise. The IA signal is the weighted contribution of the water within a set of N_d cylinders with different radii

TABLE 1 Features of ADD mapping methods

	Non-parametric	Whole ADD	Orientationally invariant	EA modeling
Assaf et al[16] (AxCaliber)	✗	✓	✗	✓
Benjamini et al[22]	✓	✓	✗	✓
Alexander et al[17] ($\text{ActiveAx}_{\text{MMWMD}}$)	✓	✗	✓	✗
Komlosh et al[18]	✓	✗	✓	✗
Proposed method ($\text{ActiveAx}_{\text{ADD}}$)	✓	✓	✓	✗

$$f_{\mathrm{IA}}\mathbf{S}_{\mathrm{IA}} = \sum_{d=1}^{N_d} \mathrm{w}_d \mathbf{S}_{\mathrm{cyl}}\left(R_d, \alpha, D_0, \Omega\right), \quad (2)$$

where w_d are the volume fractions of each cylinder, and $\mathbf{S}_{\mathrm{cyl}}$ is the dMRI signal for a cylinder with radius R_d, angles $\boldsymbol{\alpha}$ between the gradient and cylinder orientations, intrinsic diffusivity D_0 and dMRI protocol parameters Ω.[24] Clustering the cylinders into N_A bins gives

$$f_{\mathrm{IA}}S_{\mathrm{IA}} = \sum_{\mathrm{bin}=1}^{N_A} \Psi_{\mathrm{bin}} S_{\mathrm{cyl}}\left(R_{\mathrm{bin}}, \alpha, D_0, \Omega\right), \quad (3)$$

where Ψ_{bin} is the volume fraction occupied by cylinders belonging to each bin, and R_{bin} is the characteristic radius of the bin (taken to be the center of the bin).

In Equation 3, Ψ is related to the ADD[22]: if the ADD represents the relative number of cylinders with diameter within a given range (i.e., the normalized diameter histogram), then the coefficients Ψ represent the relative volume fraction occupied by those same cylinders. All further ADD references will be referring to the coefficients Ψ (i.e., the volume weighted ADD).

Equations 1 and 3 can be combined as a linear system[20-22]

$$\mathbf{y} = \mathbf{A}\mathbf{x} + \varepsilon, \quad (4)$$

Where $\mathbf{y}$ is a vector containing the measured signal $\mathbf{S}$, ε represents the acquisition noise, and $\mathbf{A}$ is a linear operator that discretizes the microstructure model of interest. In $\mathrm{ActiveAx}_{\mathrm{AMICO}}$, $\mathbf{A}$ is made of 2 sub-matrices: $\mathbf{A} = [\mathbf{A}_{\mathrm{IA}} | \mathbf{A}_{\mathrm{EA}}]$ where $\mathbf{A}_{\mathrm{IA}}$ and $\mathbf{A}_{\mathrm{EA}}$ encode the IA and EA compartments, respectively.[20] When considering N_A bins, $\mathbf{A}_{\mathrm{IA}}$ is made of N_A columns with the signal of N_A cylinders with radii R_{bin}. $\mathbf{A}_{\mathrm{EA}}$ is made of axisymmetric tensors. Cylinder and tensor orientations are set equal to the first eigenvector of the diffusion tensor fitted to the signal.[20]

As the problem is ill-posed, we solve the following regularized problem

$$\min_{\mathrm{x}\geq 0} \|\mathbf{A}\mathbf{x}\text{-}\mathbf{y}\|_2^2 + \lambda \mathfrak{R}(\mathbf{x}), \quad (5)$$

where the first term fits the solution to the data, and the second term is a regularization factor that stabilizes the solution. The coefficients $\mathbf{x}$ are the signal fractions of each column of $\mathbf{A}$ to be estimated, and can be split as $\mathbf{x} = [\mathbf{x}_{\mathrm{IA}} | \mathbf{x}_{\mathrm{EA}}]$. The normalized IA coefficients $\mathbf{x}_{\mathrm{IA}} / \sum \mathbf{x}_{\mathrm{IA}}$ therefore correspond to the estimated ADD. The mean diameter index a' can be extracted from $\mathbf{x}$ as in Daducci et al,[20] as well as the estimated IAVF.

$\mathrm{ActiveAx}_{\mathrm{AMICO}}$ uses Tikhonov regularization ($\mathfrak{R}(\mathbf{x}) = \|\mathbf{x}\|_2^2$) to estimate a'.[20,22] Inspired by Hollingsworth and Johns,[21] in this study we explored the benefits of using Laplacian regularization ($\mathfrak{R}(\mathbf{x}) = \|\mathbf{L}_2^z \mathbf{x}\|_2^2$, where $\mathbf{L}_2^z$ is the 2nd order finite difference operator with zero boundary conditions),[25] to estimate orientationally invariant and non-parametric ADDs. The proposed formulation was coined $\mathrm{ActiveAx}_{\mathrm{ADD}}$.

3 | METHODS

3.1 | Substrate design

Cylinder diameters were sampled from 22 different gamma distributions corresponding to histological samples as in Lamantia and Rakic,[1] Aboitiz et al,[2] and Alexander et al[17] (http://camino.cs.ucl.ac.uk/index.php?n=Tutorials.ActiveAx). Cylinders were randomly placed into isotropic voxels of $0.5 \times 0.5 \times 0.5$ mm^3 with IAVF of 70% and ensuring periodicity at the voxel boundaries.[26] Three illustrative substrates are shown in Figure 1. Cylinders could not be positioned for 3 of the 22 distributions (corresponding substrates only appear in the isolated IA experiments described hereafter).

3.2 | MR protocol

All substrate signals were computed using the 3-shell protocol with $\mathrm{G}_{\mathrm{max}}$ = 300 mT/m optimized for mean diameter mapping.[19] Protocol parameters were G = {300, 219, 300} mT/m, Δ = {12.1, 20.4, 16.9} ms and δ = {5.6, 7.0, 10.5} ms. Each shell had 60 directions evenly covering the unit sphere,[27] and the protocol included 70 $\mathbf{S}_0$ volumes, totaling $N_s = 250$ measurements.[19] IA and EA signals were computed separately and combined as described hereafter.

3.3 | ADD estimates using the isolated IA signal

Experiments first focused on the substrates' isolated IA signals. For each substrate, the IA signal $\mathbf{y}_{\mathrm{IA}} \in \mathbb{R}_+^{N_s}$ was computed as $\mathbf{y}_{\mathrm{IA}} = \sum_{i=1}^{N_d} w_i \mathbf{S}_{\mathrm{IA}}\left(R_i, \alpha, D^{\parallel}, \Omega\right)$ where w_i was the volume-weighted fraction of each cylinder with respect to the total IA volume $\left(w_i = \frac{R_i^2}{\sum R_i^2}\right)$ and $\mathbf{S}_{\mathrm{IA}} \in \mathbb{R}_+^{N_s}$ the analytical signal of each cylinder.[24] Intrinsic diffusivity was set to ex vivo values ($D_0 = 0.6 \times 10^{-9}$ m^2/s).[17] Fifty different noisy repetitions $\hat{\mathbf{y}}_{\mathrm{IA}} \in \mathbb{R}_+^{N_s}$ were computed for each substrate, using Rician noise and SNR = 30 in the $\mathbf{S}_0$ volumes (as typically observed in preclinical scans). Cylinders had a different orientation for each noisy repetition, homogeneously covering the unit sphere.

Coefficients $\mathbf{x}_{\mathrm{IA}}$ were estimated by solving $\min_{\mathbf{x}_{\mathrm{IA}}\geq 0} \|\mathbf{A}_{\mathrm{IA}}\mathbf{x}_{\mathrm{IA}} - \hat{\mathbf{y}}_{\mathrm{IA}}\|_2^2 + \lambda \mathfrak{R}(\mathbf{x})$ with either $\mathrm{ActiveAx}_{\mathrm{AMICO}}$ ($\mathfrak{R}(\mathbf{x}) = \|\mathbf{x}\|_2^2$) or $\mathrm{ActiveAx}_{\mathrm{ADD}}$ ($\mathfrak{R}(\mathbf{x}) = \|\mathbf{L}_2^z \mathbf{x}\|_2^2$). $\mathbf{A}_{\mathrm{IA}} \in \mathbb{R}^{N_s \times N_A}$ consisted of $N_A = 30$ cylinders with diameters equally spread in [0.5, 20] μm. Cylinders were oriented along the first eigenvector of a tensor fit to $\hat{\mathbf{y}}_{\mathrm{IA}}$, and D_0 was set to the average tensor's 1st eigenvalue ($0.607 \times 10^{-3} \pm 1 \times 10^{-5}$ mm^2/s).

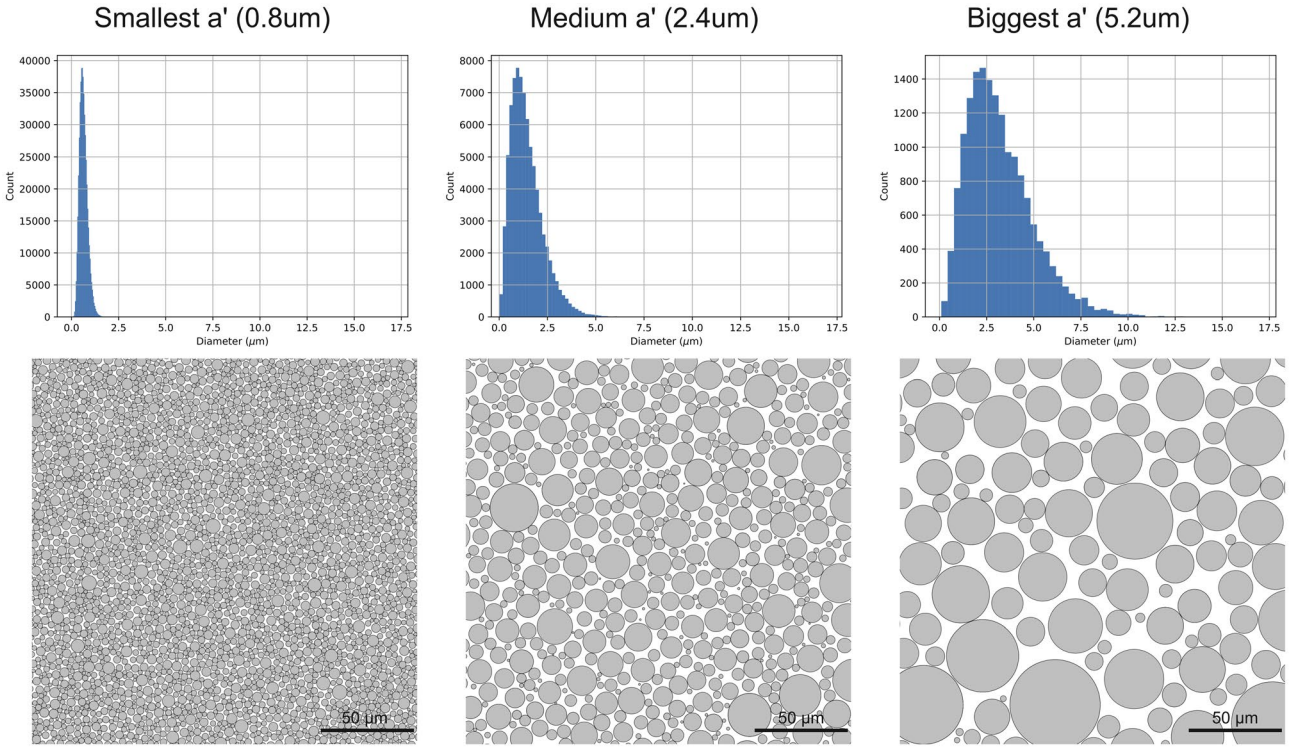

FIGURE 1 Properties of 3 representative substrates with smallest, intermediate, and biggest mean diameter index. 1st row: diameter histogram. 2nd row: partial cross-section showing some of the cylinder's positions. Black scale bars, 50 μm

Benjamini et al[22] proposed to use a submicron compartment (also known as a "stick"),[28] consisting of a tensor with zero perpendicular diffusivity, to capture the signal of cylinders with radius below the "diameter lower bound" (DLB).[19] Given a certain protocol, spins within cylinders smaller than the DLB do not move enough for the signal to decay,[19] and it appears as a tensor with zero perpendicular diffusivity. An analytical estimation was proposed by Nilsson et al,[29] which for our protocol would be $d_{min}^{(SDE)} = \left(\frac{768}{7}\frac{\bar{\sigma}D_0}{\gamma^2\delta g^2}\right)^{1/4} = 2.7$ μm (using the highest shell, SNR = 30, significance level of 5% and 1 repetition). We added the submicron compartment to the model and progressively removed from 1 to 4 columns of $\mathbf{A}_{IA}$ until the smallest cylinder was 3.19 μm. The estimated ADD was compared to the corresponding ground-truth by computing the Jensen-Shannon distance, given by $\mathrm{JSD}(P,Q) = \sum_i \frac{P_i\log(P_i+\varepsilon)+Q_i\log(Q_i+\varepsilon)}{2} - \frac{P_i+Q_i}{2}\log(\frac{P_i+Q_i+\varepsilon}{2})$, where P is the mean ADD estimated over different noise realizations, Q is the ground-truth ADD, and i is the bin index. A small $\varepsilon = 1\times10^{-16}$ was added for the log to be valid even when P_i or Q_i were zero. To test for a significant difference between the 2 regularization methods, we performed a paired t-test on 2 groups of JSDs obtained with either Tikhonov or Laplacian regularization. The number of samples was $N = 22$ JSD values in each group. λ was fixed to the value that provided the lowest JSD over all substrates.

3.4 | Adding the EA compartment

The substrates' EA signals $\mathbf{y}_{EA}$ were computed using Monte Carlo simulations. Simulations included 1 million spins with ex vivo diffusivity ($D_0 = 0.6\times10^{-9}$ m^2/s), TE = 44 ms divided in 10,000 steps (step size was 0.009 μm). Spin trajectories were elastically reflected when colliding with a cylinder, and the EA signal $\mathbf{y}_{EA}$ was computed using the phase cumulated by the spins during the ActiveAx protocol. The total substrate signal was computed as $\mathbf{y} = f_{IA} * \mathbf{y}_{IA} + (1-f_{IA}) * \mathbf{y}_{EA}$, where f_{IA} was the IAVF (set to 70%). Fifty different noisy repetitions $\hat{\mathbf{y}}$ were generated for each substrate by adding Rician noise with SNR = 30 in the $\mathbf{S}_0$ volumes. The fascicle had a different orientation in each repetition.

As the EA perpendicular diffusion is time-dependent,[30] $\mathbf{A}_{EA}$ was built using 49 time-dependent axisymmetric tensors,[31] using combinations of 7 values of $D_\infty \in [0.06\times10^{-9}, 0.42\times10^{-9}]$ m^2/s and 7 values of $\mathbf{A} \in [1.00\times10^{-14}, 5.0\times10^{-13}]$ m^2. D_∞ is the macroscopic asymptote of the diffusion coefficient, and its range corresponds to ICVFs ranging from 30 to 90%, when assuming $\mathrm{IAVF} = (D_0 - D_\infty)/D_0$.[20] $\mathbf{A}$ is related to the correlation length of the space between cylinders, and its range covers estimates obtained by Burcaw et al[30] on similar substrates (see value of sectors 2, 4, and 6 reported in Table 2 in Burcaw et al).[30] No isotropic compartment was included. The solution $\mathbf{x}$ was estimated from $\hat{\mathbf{y}}$ using

ActiveAx$_{ADD}$. Regularization was applied to the IA coefficients only, as proposed by Benjamini et al,[22] because there was no evidence to promote smoothness for EA coefficients. A paired *t*-test on JSDs obtained with either the isolated IA signals or the combined IA+EA signals was computed. Substrates for which the EA signal could not be computed were excluded from the test ($N = 19$ JSDs in each group).

To assess how other microstructure models behave with isolated IA signals, the original ActiveAx$_{MMWMD}$ model (i.e., a single cylinder) was used to estimate a' by fitting a single cylinder to the noisy IA signals $\hat{\mathbf{y}}_{IA}$ using maximum likelihood estimation. Then a' was estimated by fitting the full ActiveAx$_{MMWMD}$ model (i.e., a single cylinder and a single time-independent tensor with tortuosity constraint) to the full signal $\hat{\mathbf{y}}$, using Camino.[32]

4 | RESULTS

4.1 | ADD estimates using the isolated IA signal

For IA signals, the optimal λ was found to be 0.2 for both ActiveAx$_{AMICO}$ and ActiveAx$_{ADD}$ (Figure 2). ActiveAx$_{ADD}$ provided better mean ADD estimates compared to ActiveAx$_{AMICO}$: over the set of all substrates, ActiveAx$_{AMICO}$ had a mean JSD of 0.09 ± 0.07, which significantly decreased to 0.07 ± 0.08 (Figure 3A) when using ActiveAx$_{ADD}$ (paired *t*-test $P = 0.003$, $N = 22$ JSD values). Using Laplacian regularization promoted ADDs that were closer to the ground truth, in particular regarding small diameters. The 3rd column in Figure 3A illustrates the diameter lower bound, inherited

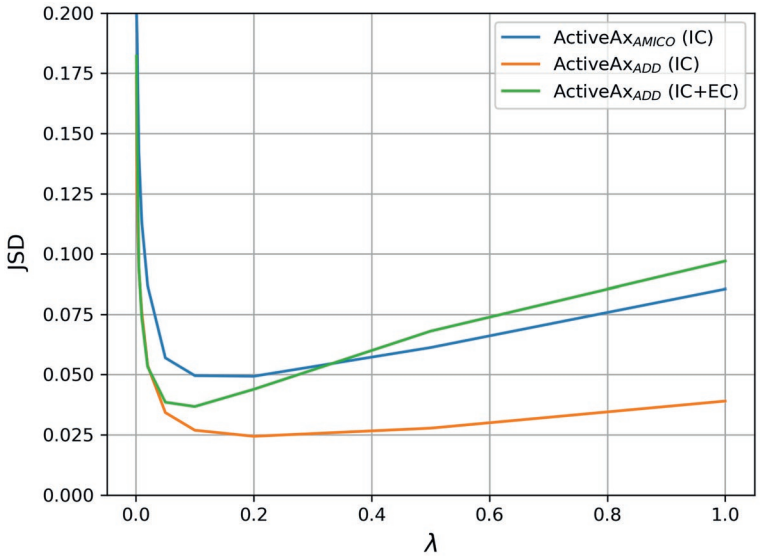

FIGURE 2 Effect of regularization weight λ on ADD accuracy (JSD) for ActiveAx$_{AMICO}$ and ActiveAx$_{ADD}$ when using isolated IA signals, and for ActiveAx$_{ADD}$ when using signals with both IA and EA components

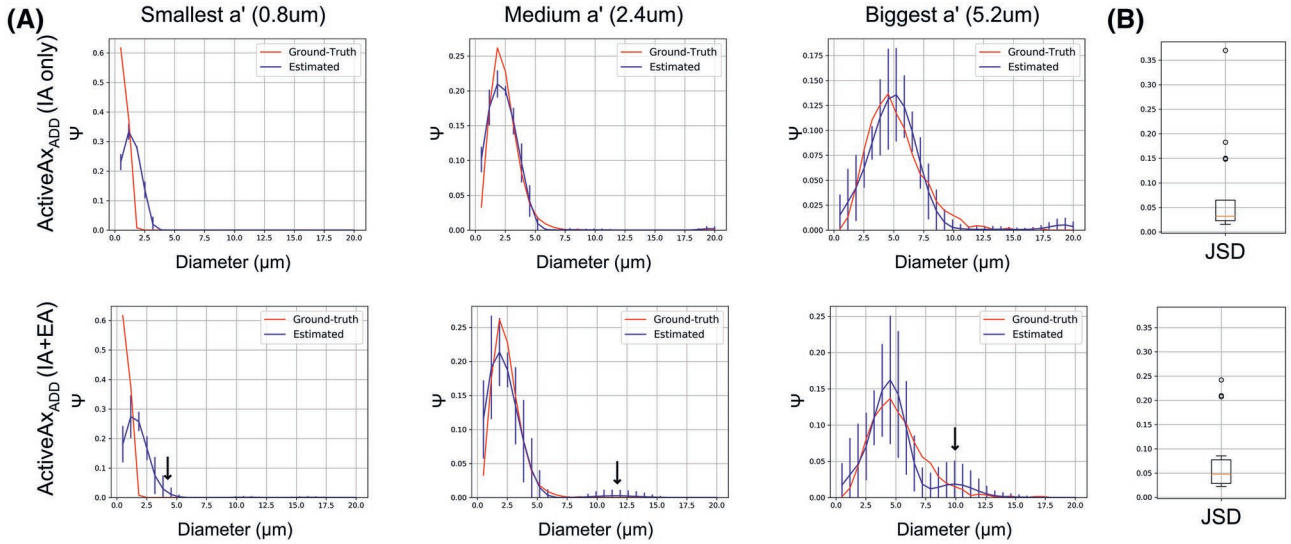

FIGURE 3 Effect of adding the EA compartment on the estimated ADD. (A) estimated ADD for 3 different substrates, using isolated IA signals (top) or signals with IA and EA components (bottom). Regions with overestimated ADD are highlighted with black arrows. (B) Boxplot of the JSD between the mean ADD and the ground-truth, when considering either the isolated IA signal (top) or both the IA and EA compartments (bottom)

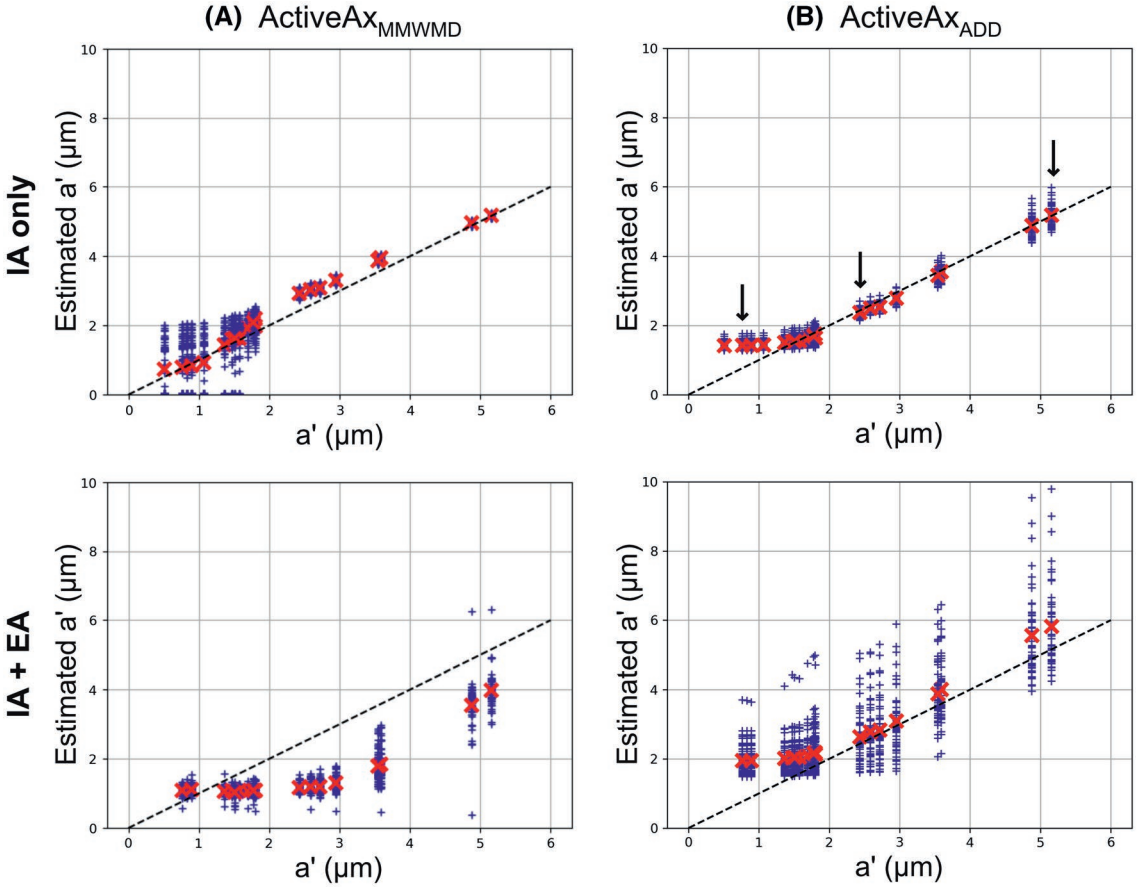

FIGURE 4 Estimates of the mean diameter index a' derived using (A) the ActiveAx$_{MMWMD}$ model, and (B) the ActiveAx$_{ADD}$ model. The first row shows estimates from the isolated IA signal whereas the second shows the effect of adding the EA compartment. Estimates of a' for each noise realization are shown with blue crosses, whereas the mean over all realizations corresponds to red crosses. The ground truth lies over the dotted black line. The 3 black arrows show the representative substrates shown in Figures 1 and 3

from the protocol. ActiveAx$_{ADD}$ promoted smooth transitions from small values for the smallest diameters to the appropriate ADD values for the diameters above the DLB. Such a trend corresponds to what has been reported in histological studies.[1,2,33,34] Adding the submicron compartment worsened ADD estimates (e.g., for some signals, the "stick" was assigned a value of 1.0, and the resulting ADD was empty).

4.2 | Adding the EA compartment

For signals with both IA and EA components, the optimal λ was found to be 0.1. However, adding the EA compartment led to spurious peaks and increased variability with respect to noise. Figure 3B shows the resulting overestimation of large diameter contributions (black arrows). The estimated IAVF ranged from 50 to 100% (not shown). Adding the EA signal significantly increased the JSD to 0.09 ± 0.08 compared to the IA estimates (paired t-test $P = 4.1 \times 10^{-5}$, $N = 19$ JSD values). Using time-independent tensors led to even higher JSD (not shown). Such results were considered to be too unstable and inaccurate to trust estimates on real PGSE data using the current 3-shell protocol, which contains a mixture of IA and EA signals.

Adding the EA signal also had a negative impact on the estimation of a' using ActiveAx$_{MMWMD}$ (Figure 4), showing that the limitation observed for ActiveAx$_{ADD}$ is shared with ActiveAx$_{MMWMD}$. Estimates of a' using ActiveAx$_{ADD}$ are shown for comparison.

5 | DISCUSSION

When considering the isolated IA compartment, we showed that ActiveAx$_{ADD}$ can provide accurate ADD estimates from an optimized PGSE protocol with G_{max} = 300 mT/m. Ill-posedness is one of the main limitations in ADD mapping. Although ActiveAx$_{ADD}$ inevitably inherits a DLB from the acquisition protocol, using Laplacian regularization with zero boundary conditions allows extrapolating ADD coefficients below this limit. ActiveAx$_{ADD}$ provided ADD estimates

that were comparable to those obtained using DDE to stabilize the ADD (see Table 2 in Benjamini et al).[22] However, $\text{ActiveAx}_{\text{ADD}}$ estimates have the added value of being orientationally invariant. Orientationally invariant ADDs might be provided from DDE data using the 5-design protocol,[35] however, to our knowledge, no study using this approach has been reported so far.

In microstructure imaging, ill-posedness is not limited to the IA compartment. Models are also subject to degeneracy between compartments.[36] In our experiments, ADDs estimated from signals containing both IA and EA contributions contained spurious peaks and had increased variability with respect to noise. The IAVF was either underestimated or overestimated, which indicated that part of the IA signal was captured by the EA model, and vice-versa. The same observation was made for $\text{ActiveAx}_{\text{MMWMD}}$, which showed that $\text{ActiveAx}_{\text{ADD}}$'s difficulty to disentangle IA and EA contributions is inherited from the $\text{ActiveAx}_{\text{MMWMD}}$ model. As the PGSE protocol used in the experiments was optimized according to the $\text{ActiveAx}_{\text{MMWMD}}$ model (a single cylinder with a time-independent tensor), other PGSE parameters might be required to properly disentangle the 2 compartments. The advantage of other sequences like oscillating gradients[37] or DDE might be an enhanced separation between IA and EA compartments,[38] rather than the decreased similarity between cylinders. Proposed orientationally invariant methods should be thoroughly tested and evaluated before they are applied on real signals.[39,40]

$\text{ActiveAx}_{\text{ADD}}$ can nevertheless be applied to IA signals isolated from WM samples, ignoring the EA compartment. Indeed, Hollingsworth and Johns[21] were able to obtain experimental results by focusing on oil droplets in water, isolating the oil signal by following the attenuation of the aromatic peak in the NMR spectrum of their samples. Isolated IA signals can be obtained from WM samples using diffusion dMRI acquired at very high b-values or using magnetic resonance spectroscopy (dMRS). Indeed, high-end scanners like the Connectom Scanner[41] allow performing dMRI acquisitions at b-values that are theoretically high enough to neglect the EA signal.[42] The protocol should nevertheless be adapted to in vivo diffusivity and careful experiments should be conducted to ensure that the EA compartment can effectively be ignored (e.g., Monte Carlo simulations). On the other hand, dMRS sequences allow isolating the diffusion signal for specific metabolites like *N*-acetyl-aspartate and glutamate, which are physically restrained to the IA space.[43] In vivo metabolites have diffusivities similar to ex vivo water, which matches our simulations.[43]

Other WM features should be taken into consideration when applying $\text{ActiveAx}_{\text{ADD}}$ on real data. First, our simulations did not include dispersion and/or undulation of axons. This feature could be included in the model[44] or factored out of the signal using b-tensor encoding[45] or the spherical mean technique.[46] Then, our simulations didn't include the effect of compartment specific T_1 and T_2 relaxation times, which should be included in the model if they are different between compartments. The IA and EA compartments have been shown to have different intrinsic diffusivities, which are not easily determined,[36] but should be included in the model to avoid bias.

6 | CONCLUSION

Experiments showed that non-parametric and orientationally invariant ADDs can be reliably reconstructed from PGSE data using $\text{ActiveAx}_{\text{ADD}}$. The method inherits common limitations of current microstructure models, in particular the DLB and the difficulty of disentangling IA and EA contributions. The proposed formulation is therefore of interest for methods that provide isolated IA signals (e.g., PGSE data acquired at high b-values or dMRS data). Further work is nevertheless required before applying the method to real data containing a mixture of both compartments. In particular we require the formulation of a protocol or sequence, as well as an appropriate EA model, that allows disentangling properly the 2 compartments.

ACKNOWLEDGMENTS

We would like to thank Dr. Anna Auría for her feedback on experiment design and code implementation, as well as Thomas Yu for proofreading the manuscript. This project was funded by the Swiss National Science Foundation (SNSF), under grant 31003A_157063, and supported by EPFL through the use of the facilities of its Scientific IT and Application Support Center.

ORCID

David Romascano https://orcid.org/0000-0002-8823-9176
Muhamed Barakovic https://orcid.org/0000-0001-8557-9223
Jonathan Rafael-Patino https://orcid.org/0000-0002-8960-5465
Tim Bjørn Dyrby https://orcid.org/0000-0003-3361-9734
Jean-Philippe Thiran https://orcid.org/0000-0003-2938-9657
Alessandro Daducci https://orcid.org/0000-0002-4677-6678

REFERENCES

1. Lamantia AS, Rakic P. Cytological and quantitative characteristics of four cerebral commissures in the rhesus monkey. *J Comp Neurol*. 1990;291:520–537.
2. Aboitiz F, Scheibel AB, Fisher RS, Zaidel E. Fiber composition of the human corpus callosum. *Brain Res*. 1992;598:143–153.

3. Tasaki I, Ishii K, Ito H. On the relation between the conduction-rate, the fiber-diameter and the internodal distance of the medullated nerve fiber. *Jpn J Med Sci III, Biophys*. 1943;9: 189–199.
4. Waxman S. Determinants of conduction velocity in myelinated nerve fibers. *Muscle Nerve*. 1980;3:141–150.
5. Colello RJ, Pott U, Schwab ME. The role of oligodendrocytes and myelin on axon maturation in the developing rat retinofugal pathway. *J Neurosci*. 1994;14:2594–2605.
6. Trapp BD, Peterson J, Ransohoff RM, Rudick R, Mörk S, Bö L. Axonal transection in the lesions of multiple sclerosis. *N Engl J Med*. 1998;338:278–285.
7. Lovas G, Szilagyi N, Majtenyi K, Palkovits M, Komoly S. Axonal changes in chronic demyelinated cervical spinal cord plaques. *Brain*. 2000;123:308–317.
8. Evangelou N, Konz D, Esiri MM, Smith S, Palace J, Matthews PM. Size-selective neuronal changes in the anterior optic pathways suggest a differential susceptibility to injury in multiple sclerosis. *Brain*. 2001;124:1813–1820.
9. DeLuca GC, Ebers GC, Esiri MM. Axonal loss in multiple sclerosis: a pathological survey of the corticospinal and sensory tracts. *Brain*. 2004;127:1009–1018.
10. Cluskey S, Ramsden D. Mechanisms of neurodegeneration in amyotrophic lateral sclerosis. *Mol Pathol*. 2001;54:386–392.
11. Le NTT, Chang L, Kovlyagina I, et al. Motor neuron disease, TDP-43 pathology, and memory deficits in mice expressing ALS-FTD-linked UBQLN2 mutations. *Proc Natl Acad Sci USA*. 2016;113:E7580–E7589.
12. Badea A, Kane L, Anderson RJ, et al. The fornix provides multiple biomarkers to characterize circuit disruption in a mouse model of Alzheimer's disease. *NeuroImage*. 2016;142:498–511.
13. Dollé JP, Morrison B, Schloss RS, Yarmush ML, Yarmush ML. Brain-on-a-chip microsystem for investigating traumatic brain injury: axon diameter and mitochondrial membrane changes play a significant role in axonal response to strain injuries. *Technology (Singap World Sci)*. 2014;2:106.
14. Budde MD, Frank JA. Neurite beading is sufficient to decrease the apparent diffusion coefficient after ischemic stroke. *Proc Natl Acad Sci USA*. 2010;107:14472–14477.
15. Benjamini D, Katz Y, Nevo U. A proposed 2D framework for estimation of pore size distribution by double pulsed field gradient NMR. *J Chem Phys*. 2012;137:224201.
16. Assaf Y, Blumenfeld-Katzir T, Yovel Y, Basser PJ. AxCaliber: a method for measuring axon diameter distribution from diffusion MRI. *Magn Reson Med*. 2008;59:1347–1354.
17. Alexander DC, Hubbard PL, Hall MG, et al. Orientationally invariant indices of axon diameter and density from diffusion MRI. *NeuroImage*. 2010;52:1374–1389.
18. Komlosh ME, Özarslan E, Lizak MJ, et al. Mapping average axon diameters in porcine spinal cord white matter and rat corpus callosum using d-PFG MRI. *NeuroImage*. 2013;78:210–216.
19. Dyrby T, Sogaard L, Hall M, Ptito M, Alexander DC. Contrast and stability of the axon diameter index from microstructure imaging with diffusion MRI. *Magn Reson Med*. 2013;70: 711–721.
20. Daducci A, Canales-Rodríguez EJ, Zhang H, Dyrby TB, Alexander DC, Thiran JP. Accelerated microstructure imaging via convex optimization (AMICO) from diffusion MRI data. *NeuroImage*. 2015;105:32–44.
21. Hollingsworth KG, Johns ML. Measurement of emulsion droplet sizes using PFG NMR and regularization methods. *J Colloid Interface Sci*. 2003;258:383–389.
22. Benjamini D, Komlosh ME, Holtzclaw LA, Nevo U, Basser PJ. White matter microstructure from nonparametric axon diameter distribution mapping. *NeuroImage*. 2016;135:333–344.
23. Assaf Y, Freidlin RZ, Rohde GK, Basser PJ. New modeling and experimental framework to characterize hindered and restricted water diffusion in brain white matter. *Magn Reson Med*. 2004;52:965–978.
24. van Gelderen P, DesPres D, van Zijl PC, Moonen CT. Evaluation of restricted diffusion in cylinders. Phosphocreatine in rabbit leg muscle. *J Magn Reson B*. 1994;103:255–260.
25. Hansen PC. *Discrete inverse problems: insight and algorithms*. Universal City: Society for Industrial and Applied Mathematics; 2010:226.
26. Hall MG, Alexander DC. Convergence and parameter choice for Monte-Carlo simulations of diffusion MRI. *IEEE Trans Med Imaging*. 2009;28:1354–1364.
27. Caruyer E, Lenglet C, Sapiro G, Deriche R. Design of multishell sampling schemes with uniform coverage in diffusion MRI. *Magn Reson Med*. 2013;69:1534–1540.
28. Panagiotaki E, Schneider T, Siow B, Hall MG, Lythgoe MF, Alexander DC. Compartment models of the diffusion MR signal in brain white matter: a taxonomy and comparison. *NeuroImage*. 2012;59:2241–2254.
29. Nilsson M, Lasic S, Drobnjak I, Topgaard D, Westin CF. Resolution limit of cylinder diameter estimation by diffusion MRI: the impact of gradient waveform and orientation dispersion. *NMR Biomed*. 2017;30:e3711.
30. Burcaw LM, Fieremans E, Novikov DS. Mesoscopic structure of neuronal tracts from time-dependent diffusion. *NeuroImage*. 2015;114:18–37.
31. De Santis S, Jones DK, Roebroeck A. Including diffusion time dependence in the extra-axonal space improves in vivo estimates of axonal diameter and density in human white matter. *NeuroImage*. 2016;130:91–103.
32. Cook P, Bai Y, Nedjati-Gilani S, et al. Camino: open-source diffusion-MRI reconstruction and processing. In Proceedings of the 14th Annual Meeting of the ISMRM, Seattle, WA, 2006. Abstract 2759.
33. Barazany D, Basser PJ, Assaf Y. In vivo measurement of axon diameter distribution in the corpus callosum of rat brain. *Brain*. 2009;132:1210–1220.
34. Liewald D, Miller R, Logothetis N, Wagner HJ, Schüz A. Distribution of axon diameters in cortical white matter: an electron-microscopic study on three human brains and a macaque. *Biol Cybern*. 2014;108:541–557.
35. Jespersen SN, Lundell H, Sønderby CK, Dyrby TB. Orientationally invariant metrics of apparent compartment eccentricity from double pulsed field gradient diffusion experiments. *NMR Biomed*. 2013;26:1647–1662.
36. Jelescu IO, Veraart J, Fieremans E, Novikov DS. Degeneracy in model parameter estimation for multi-compartmental diffusion in neuronal tissue. *NMR Biomed*. 2016;29:33–47.
37. Drobnjak I, Zhang H, Ianus A, Kaden E, Alexander DC. PGSE, OGSE, and sensitivity to axon diameter in diffusion MRI: insight from a simulation study. *Magn Reson Med*. 2016;75: 688–700.

38. Coelho S, Pozo JM, Jespersen SN, Jones DK, Frangi AF. Double diffusion encoding prevents degeneracy in parameter estimation of biophysical models in diffusion MRI. arXiv preprint arXiv. 2018:180905059.
39. Benjamini D, Nevo U. Estimation of pore size distribution using concentric double pulsed-field gradient NMR. *J Magn Reson*. 2013;230:198–204.
40. Benjamini D, Komlosh ME, Basser PJ, Nevo U. Nonparametric pore size distribution using d-PFG: comparison to s-PFG and migration to MRI. *J Magn Reson*. 2014;246:36–45.
41. Jones DK, Alexander DC, Bowtell R, et al. Microstructural imaging of the human brain with a 'super-scanner': 10 key advantages of ultra-strong gradients for diffusion MRI. *NeuroImage*. 2018;182:8–38.
42. Veraart J, Fieremans E, Novikov DS. On the scaling behavior of water diffusion in human brain white matter. *NeuroImage*. 2019;185:379–387.
43. Palombo M, Ligneul C, Hernandez-Garzon E, Valette J. Can we detect the effect of spines and leaflets on the diffusion of brain intracellular metabolites? *NeuroImage*. 2017;182:283–293.
44. Zhang H, Hubbard PL, Parker GJM, Alexander DC. Axon diameter mapping in the presence of orientation dispersion with diffusion MRI. *NeuroImage*. 2011;56:1301–1315.
45. Westin CF, Szczepankiewicz F, Pasternak O, et al. Measurement tensors in diffusion MRI: generalizing the concept of diffusion encoding. *Med Image Comput Comput Assist Interv*. 2014;17:209–216.
46. Kaden E, Kruggel F, Alexander DC. Quantitative mapping of the per-axon diffusion coefficients in brain white matter. *Magn Reson Med*. 2016;75:1752–1763.

How to cite this article: Romascano D, Barakovic M, Rafael-Patino J, Dyrby TB, Thiran J-P, Daducci A. ActiveAx$_{ADD}$: Toward non-parametric and orientationally invariant axon diameter distribution mapping using PGSE. *Magn Reson Med*. 2020;83:2322–2330. https://doi.org/10.1002/mrm.28053